Photoactive electrically switchable van der Waals semiconductor NbOl₂

Cite as: Appl. Phys. Lett. **119**, 033103 (2021); doi: 10.1063/5.0052941 Submitted: 2 April 2021 · Accepted: 14 July 2021 ·

Published Online: 21 July 2021







Zhizhong Chen, Yang Hu, 📵 Lifu Zhang, Jie Jiang, 🕞 Ryan Hawks, 📵 and Jian Shi^{a)} 🕞

AFFILIATIONS

Department of Materials Science and Engineering, Rensselaer Polytechnic Institute, Troy, New York 12180, USA

^{a)}Author to whom correspondence should be addressed: shij4@rpi.edu

ABSTRACT

Room temperature van der Waals ferroelectric materials whose ferroelectricity may survive down to atomic layer limit are highly desirable for device miniaturization. In this article, we present the optically active reconfigurable room temperature rectification in a recently predicted ferroelectric van der Waals material NbOI₂. NbOI₂ devices with a thin (\sim 17-unit cells) single crystalline channel and inert graphite electrodes were assembled into two-terminal devices which showed >100 × photoresponse to 405 nm laser. By DC poling on a 1- μ m-channel NbOI₂ device, the photocurrent changed from symmetric to single-Schottky-diode type. The polarity of such rectification can be switched back and forth by DC poling along opposite directions. Such reconfigurability evidences the existence of in-plane room temperature ferroelectricity in thin NbOI₂ and its potential in nonvolatile optoneuromorphic computing and nonvolatile technologies.

Published under an exclusive license by AIP Publishing. https://doi.org/10.1063/5.0052941

Innovations in materials provide a strong impetus in the development of nonvolatile electronic devices and the extension of Moore's law at large, specifically device miniaturization, high operation speed and reliability, reduction in energy consumption, etc. The depolarization field of conventional ferroelectrics remains a major challenge for the miniaturization of ferroelectric memory devices. 1,2 The use of layered ferroelectrics beyond perovskite oxides not only enables robust ferroelectricity down to a few-atomic-layers limit, but also triggers innovative device architectures, such as ferroelectric semiconductor field effect transistor.³ On the other hand, the integration of optically active materials (e.g., semiconductors or organic dyes) into integrated circuits could potentially alleviate technical issues, such as crosstalk, resistor-capacitor delay, and Joule heating, by utilizing photons as another information carrier, as witnessed by the recent demonstrations of artificial synapse or optoelectronic logic enabled by optically modulated Schottky barriers.4

The search for van der Waals (vdW) ferroelectric semiconductors with ferroelectric ordering, even in atomically thin layers, being optically active within the visible regime and high Curie temperature has identified a handful of candidates, mainly among chalcogenides, e.g., α -In₂Se₃, group-IV monochalcogenide (GeS, SnTe, SnS, and SnSe), 1T-MoS₂ monolayers, etc.^{3,6–10} Very recently, a family of vdW oxyhalides NbOX₂ (X = Cl, Br, I) was predicted to be ferroelectric with spontaneous polarization \sim 20 μ C cm⁻², optical bandgap 1.6–1.9 eV, and potentially above-room temperature ferroelectric ordering down

to monolayer limit.¹¹ Not only oxyhalides may inherit the chemical abundance and the ease of fabrication from the oxide nature, but also their split-anion composition can render interesting symmetry-induced physical phenomena beyond ferroelectricity.¹² Despite the synthesis of bulk NbOX₂ in the 1960s, the experimental study on their electronic or optical properties has remained absent. ^{13–15}

Here, we report the optically active and electric-field switchable Schottky barriers in ultrathin vdW NbOI $_2$. We present the observation of switchable rectification in double-Schottky-diode devices upon electric field poling. The switching is attributed to the modulation of Schottky barrier heights by interface dipoles, evidencing the room temperature in-plane ferroelectricity in thin NbOI $_2$ sheet.

At room temperature, NbOI₂ crystallizes into a monoclinic phase, with a = 7.52 Å, b = 3.924 Å, c = 15.036 Å, and β = 103.3°, assigned to a space group C2 [Fig. 1(a)]. The Nb-O-I octahedra show both edge-sharing and corner-sharing co-ordinations and are separated by a vdW gap of ~3 Å parallel to (001). Although the ferroelectricity in NbOI₂ was not experimentally verified in earlier works, the polar phase by a recent theoretical study turns out highly consistent with the room temperature structure obtained from early x-ray diffraction (XRD) studies. 11,14 Calculated phonon spectrum of NbOX₂ indicates that the ferroelectric ordering along b axis stems from the displacement of Nb, as shown by the orange arrow in Fig. 1(a) right sketch. The crystal structures of NbOX₂ and their alloyed phases are supposed to be similar to NbOI₂. In this work, NbOI₂ bulk crystals

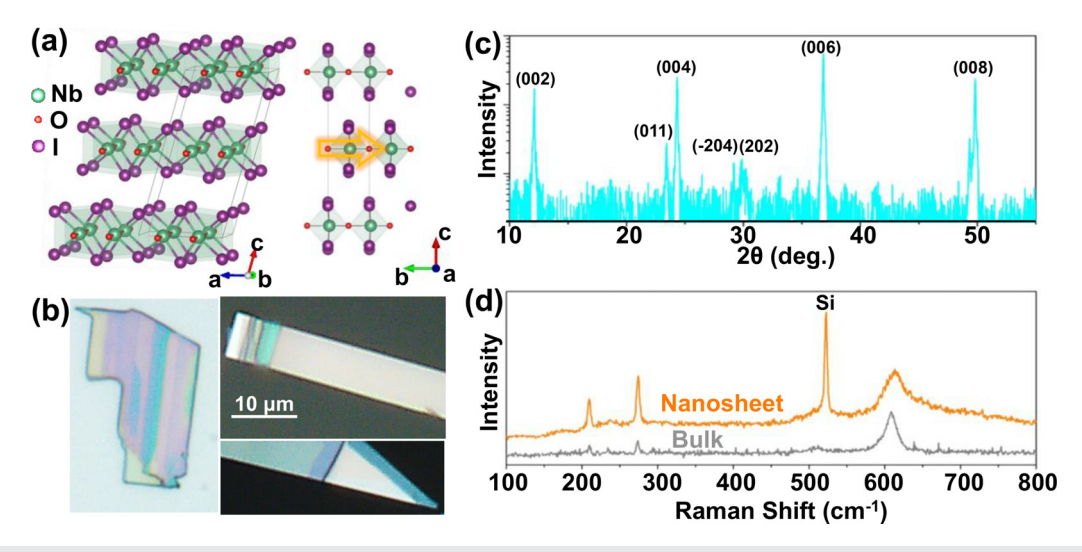


FIG. 1. Structure and characterizations of NbOl₂ single crystals. (a) Structure of NbOl₂ in room temperature monoclinic phase. The polar displacement of Nb is highlighted by the orange arrow. (b) Optical images of exfoliated NbOl₂ nanosheets. The three images are under the same magnification. (c) XRD of ground NbOl₂ bulk crystals. (d) Raman spectra from NbOl₂ bulk crystals and nanosheets. The peak at \sim 524 cm⁻¹ is from silicon substrate. The three peaks at 209, 273, and 611 cm⁻¹ are from NbOl₂.

were synthesized by a chemical vapor transport method (see "Methods" in the supplementary material). As-synthesized NbOI₂ bulk crystals are \sim 1 mm in size, showing a black color and shiny facets, consistent with previous reports. Energy-dispersive x-ray spectroscopy (EDX) analysis also indicates a Nb:I = 1:2 atomic ratio. As expected, the crystals can be easily exfoliated by scotch tapes and transferred onto various substrates with their optical images shown in Fig. 1(b). The rainbow-like colors on the flakes or their edges indicate the formation of terrace structure, consistent with the cracking of layered materials during exfoliation. In some cases, gray and semitransparent layers can be observed on the edges of exfoliated crystals, as shown in Fig. 1(b), lower-right, and supplementary material Fig. S1. The exfoliated crystals showed no observable degradation after exposing to ambient condition for a few weeks. Based on atomic force microscopy (AFM) in Fig. S1, the smallest thickness we can obtain is \sim 4.5 nm, which can be assigned to three layers of unit cells. XRD on ground NbOI₂ crystals is shown in Fig. 1(c) and turns out highly consistent with the structure reported earlier. ¹⁴ The strong (002n) peaks indicate that the crystals prefer to distribute with the vdW planes oriented horizontally even after grinding. The Raman spectra of NbOI2 bulk crystal and nanosheets transferred to a Si substrate are shown in Fig. 1(d) (see "Methods" in the supplementary material). In both cases, three Raman peaks can be observed at 209, 273, and 611 cm⁻¹ Although a theoretical reference on the Raman spectrum of NbOX₂ is still lacking, the observed peaks cannot be assigned to either Nb₂O₅ or NbO₂. ¹⁶⁻¹⁹ Nevertheless, the two sharp peaks at 209 and 273 cm⁻¹ are energetically close to the Raman peaks observed in Nb2O5, which are assigned to the vibration of the whole Nb-O octahedron. 16 Therefore, the structural and optical studies so far have confirmed the synthesis of phase-pure NbOI₂.

For transport and optoelectronic studies, exfoliated NbOI₂ and graphite were assembled into two-channel planar devices (see "Methods" in the supplementary material). Here, exfoliated graphite sheets were used as electrodes for their chemical stability and mechanical flexibility. The optical image and a sketch of device 1 are shown in

Figs. 2(a) and 2(b), respectively. Here, a rectangular NbOI₂ crystal was transferred onto the top of two graphite (Gr.) sheets, yielding a channel length of \sim 25 μ m and width of \sim 8 μ m. The dark and photocurrent (illuminated by fluorescent lamps, \sim 10 W m⁻²) of device 1 are compared in Fig. 2(c). Despite a \sim 30-fold increase in current upon illumination, the line shape of the two curves is rather similar. A change in the slope of I–V curves can be observed around +1.5 V bias, which is an indicative of a possible change in conduction mechanism.

In general, the electron emission through a single Schottky barrier with a bias-dependent permittivity of insulator yields

$$J = A^* T^2 e^{-\frac{q\Phi_B}{k_B T}} e^{\frac{\sqrt{q^3 E/4\pi\epsilon_i}}{k_B T}},\tag{1}$$

where J is the current density, E is the electric field intensity defined as the voltage applied to the device divided by the distance between electrodes, A^* is the Richardson constant, q is the elementary charge, k_B is the Boltzmann constant, ϵ_i is the insulator dynamic permittivity, and Φ_B is the Schottky barrier height.²⁰ When the Schottky emission dominates, one would expect a straight line in a $\log |I| - \sqrt{|V|}$ plot. In the presence of trap states, space-charge-limited (SCL) conduction would dominate, yielding $I \propto V^n$, where n > 1 (n = 1 indicates Ohmic contact). Therefore, if SCL conduction dominates, a log |I| - |V| plot would yield a straight line with its slope n > 1. The photocurrent given in Fig. 2(c) is replotted as Figs. 2(d) and 2(e) so as to verify the possible Schottky or SCL conduction. The $\log |I| - |V|$ plot in Fig. 2(d) mostly falls onto different straight lines, indicating that the conduction with -5 to 0 V and 0 to +2.5 V is dominated by trap filling processes (i.e., SCL). When bias exceeds $\sim +2.5 \,\mathrm{V}$, the $\log |I| - \sqrt{|V|}$ re-plot yields a straight line, indicating the strong Schottky emission in this regime. Such SCL-dominated conduction in low bias regime and transition to other mechanisms at high bias regime are common in oxide ferroelectrics.²¹ The Ohmic contact between metal and vdW semiconductor is rather challenging to achieve due to the presence of vdW gap, the high structural anisotropy, and the possible formation of interface defects or Fermi level pinning.²² In device 1, since the dimension of the

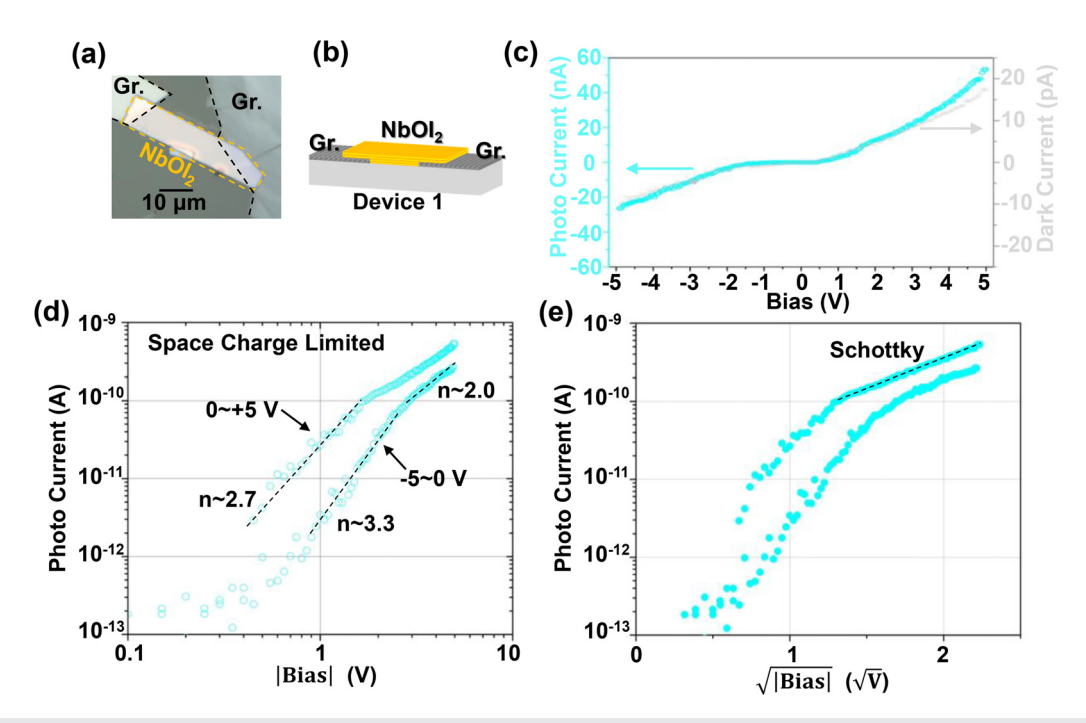


FIG. 2. Transport characteristics and photoresponse of NbOl₂ device 1. (a) and (b) Optical image and structure sketch of device 1. (c) I–V curves of NbOl₂ device 1 measured in the dark or illuminated by \sim 10 W m⁻² lamp light. (d) Re-plot of the photocurrent of device 1 using log|I| - |V|. (e) Re-plot of the photocurrent of device 1 using log $|I| - \sqrt{|V|}$.

graphite–NbOI $_2$ interfaces is comparable to that of the channel, the channel resistance might become comparable to those from the interfaces. In this regard, the origin of the trap states observed in the low bias regime of device 1 becomes hard to identify. In the presence of interface trap states, light illumination introduces mobile carriers and might change the Schottky barrier height. In device 1, however, the similar slope of the I–V curves of photo and dark currents when bias is above $+3\,\mathrm{V}$ indicates the similar Schottky barrier heights in these two scenarios and can possibly exclude the interface traps as the main origin of the trap states in device $1.^{23}$

To probe the ferroelectricity, NbOI2 microcrystals were pressed into a ceramic pellet (diameter 6.35 mm and thickness \sim 0.1 mm). By applying the double wave method, a P-E loop was obtained, yielding remnant polarization \sim 50 μ C/cm², qualitatively consistent with prediction (see "Methods," Fig. S3, and supplementary material note 1 for details). 11 Due to the fundamental challenge in measuring the P-E hysteresis loop of lateral nanosheet devices (dominant capacitance is parasitic since most electric fields do not pass through the device, see the supplementary material note 2 for details), the ferroelectricity of the channel material is often probed indirectly by monitoring the change of Schottky barrier heights upon electric poling. 24,25 Briefly, the bound charge at the surface of a properly poled in-plane ferroelectric material would contribute to electric displacement, change the barrier height at metal-ferroelectric interfaces, and, in turn, adjust the I-V rectification of the device. Therefore, we fabricated the device 2 with a much shorter channel, Fig. 3(a). Based on the color of the exfoliated NbOI₂ nanosheets transferred onto SiO₂/Si wafer (Fig. S1), the thickness of the NbOI2 crystal in device 2 is 20-30 nm, corresponding to 13-20-unit cells. In device 2, the two graphite electrodes are on top

and beneath the NbOI $_2$ nanosheets, and a narrow channel is intentionally introduced so that (i) the channel length can be reduced to $\sim 1~\mu m$, and potential breakdown of the air gap between electrodes can be avoided; (ii) the electrodes surrounding both top and bottom surfaces and the edges of the NbOI $_2$ nanosheet provide sufficient screening charges; and (iii) the reduction in channel length and channel resistance facilitates the exploration of the potential in-plane ferroelectricity and the conduction mechanism in NbOI $_2$.

The photoresponse transient of device 2 is shown in Fig. 3(b). When a -5 V bias was applied, the current increased by 130 fold when the channel region was illuminated (405 nm diode laser, 5 mW, spot diameter \sim 2 mm, unfocused). Both rise and fall current transients can be captured by the following bi-exponential model:

$$I(t) = I_0 + I_1 e^{\frac{t-t_0}{\tau_1}} + I_2 e^{\frac{t-t_0}{\tau_2}},$$
 (2)

where I_0 indicates a constant background current. The increment from photocurrent is decomposed into two parts with their prefactors I_1 and I_2 . The time constants are indicated by τ_1 and τ_2 , respectively. As compared in Fig. 3(b), the instant response in rise/fall of photocurrent is dominated by time constants 0.43 and 0.47 s, respectively. Following this instant response, the rise/fall transients are dominated by two longer time constants, 10.53 and 4.65 s, respectively. Similar biexponential profiles were observed in device 1 except that the time constants are much longer [Fig. S2(b)]. The short- and long-time constants can be ascribed to the carrier extraction near electrodes and the carrier drifting inside the channel, respectively. The long-time constants might partly come from the intrinsic electronic band structure of NbOI₂, which carries a complex optical transitions and carrier

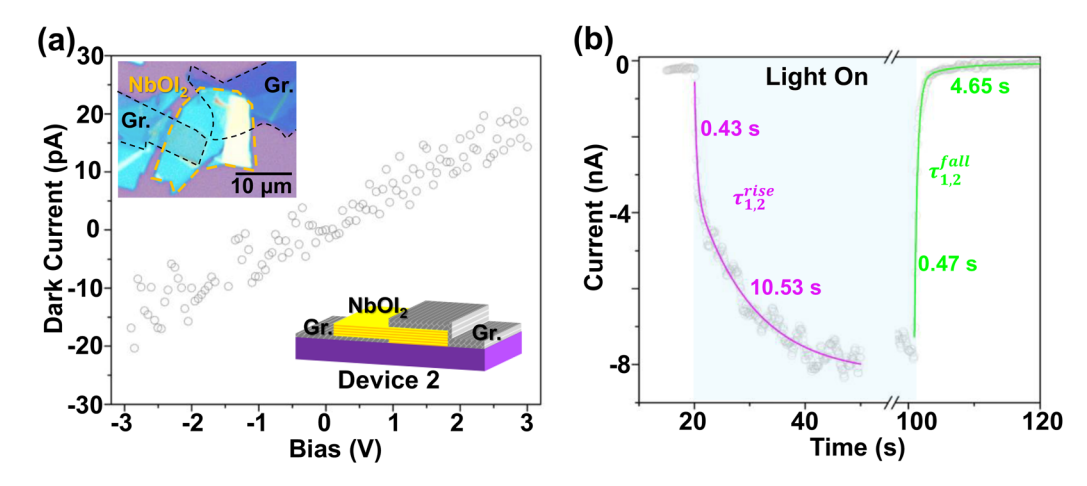


FIG. 3. Photoresponse of device 2. (a) Near symmetric and linear dark current of device 2. The insets show the optical image and structure of the device. The channel length is \sim 1 μ m. (b) Photoresponse transient under -5 V bias.

relaxations (see the supplementary material note 3 for details). ¹¹ The bi-exponential decay of photoconductivity may be suitable for emulating the spike-timing-dependent plasticity of biological synapse with a potential application in photonic synaptic devices. ⁵ The arguably symmetry-induced slow photoconductivity transient also offers higher controllability and repeatability in device design/fabrication compared to extrinsically induced modulations.

The photocurrent of device 2 (illuminated by 405 nm diode laser, 5 mW, spot diameter $\sim\!2$ mm, unfocused) turns out nonlinear but symmetric, Fig. 4(a), which is completely different from the nearlinear dark I–V response shown in Fig. 3(a). The current from two back-to-back symmetric Schottky diodes with a negligible channel resistance yields

$$J = A^* T^2 \exp\left(-\frac{\Phi_B}{k_B T}\right) \frac{\sinh\left(\frac{eV}{2k_B T}\right)}{\cosh\left(\frac{eV}{2nk_B T}\right)},$$
(3)

where n represents the ideality factor of Schottky barrier, and other parameters carry the same meanings as in Eq. (1). As shown in the inset of Fig. 4(a), the photocurrent (hereafter named stage 1) can be fitted using Eq. (3), yielding an ideality factor of n = 1.068, rather close to unity. It should be noted that fitting using Eq. (3) cannot provide the exact barrier height. Therefore, when illuminated, the channel resistance of device 2 is reduced significantly such that the I–V characteristics become dominated by the Schottky barriers at interfaces alone. By temperature-dependent I–V measurements using the ceramic pellet device, the Cu–NbOI₂ Schottky barrier height is estimated to be $\sim 0.85 \, \text{V}$ (details are in Fig. S6 and supplementary material note 4).

To verify the re-configurability of interfacial Schottky barriers, device 2 was poled by $+20 \, \text{V}$ for 10 min in the dark (nominal electric field intensity $\sim\!200 \, \text{kV} \, \text{cm}^{-1}$), yielding stage 2 shown by the orange curve in Fig. 4(b). Interestingly, the photocurrent of stage 2 is highly asymmetric with a knee voltage around $+2.2 \, \text{V}$, highly similar to that from a single Schottky diode. In addition, the photocurrent of stage 2 at $+3 \, \text{V}$ bias is about ten times that of stage 1 under the same bias, while the photocurrent in the reverse-biased cycles of stages 1 and 2 is

similar. When device 2 was poled by $-20 \,\mathrm{V}$ for $10 \,\mathrm{min}$ in the dark [yielding stage 3, shown by the aquamarine curve in Fig. 4(b)], the I-V curve inherits the line shape from stage 2 except the opposite polarity. Again, the I-V curve of stage 3 highly resembles that from a single Schottky diode with a knee voltage $\sim -1.6 \,\mathrm{V}$. As shown in Fig. 4(c), after re-plotting the photocurrent in stage 2 as $\log |I| - \sqrt{|V|}$ (based on Schottky emission, the main plot) or $\log |I| - |V|$ (based on SCL conduction, the inset), the I-V characteristics of the reverse-biased region and +2 to +3 V region can be captured by the Schottky emission mechanism because these two parts fall precisely onto the straight-dashed lines drawn in the main plot. For 0 to +1 V, the SCL re-plot yields a straight line, indicating a trap filling in this region. The +1 to +2 V part, covering to knee voltage or the "turn on process," cannot be well captured by either SCL or Schottky emission and might be attributed to a defect-related complicated process. Similar trends are expected in stage 3. The trap filling process in the low-biased region may also explain the slight deviation of the I-V curve from Eq. (3) in stage 1.

The switchable rectifications observed in stages 1, 2, and 3 of device 2 can be explained by the switchable polarizations in NbOI₂ channel, which are enabled by its in-plane ferroelectricity. 21,24,27,28 As the energy band diagram in Fig. 4(a) shows, in the virgin state (stage 1), the ferroelectric dipoles of NbOI₂, supposedly along [010], are randomly oriented, rendering no net bound charges on the surfaces. Therefore, symmetric Schottky barriers Φ_B are formed on the two graphite-NbOI2 surfaces with the barrier height determined by the intrinsic band edge energies and the Fermi level of both materials. As sketched in Fig. 4(d), the subsequent poling aligned the ferroelectric dipoles and led to the accumulation of un-neutralized bound charges on NbOI2 surfaces, eventually raised/lowered the Schottky barriers across each interface by Φ_P . As a result, the I-V characteristics in stages 2 and 3 can be described as two asymmetric back-to-back Schottky diodes connected in series. The modulation on barrier heights also explains the much higher photocurrent of the forwardbiased cycle of stage 2 (or the reverse-biased cycle of stage 3) than that of stage 1. The fact that the single-Schottky-barrier-based log|I| $-\sqrt{|V|}$ re-plot does capture the main characteristics of stage 2

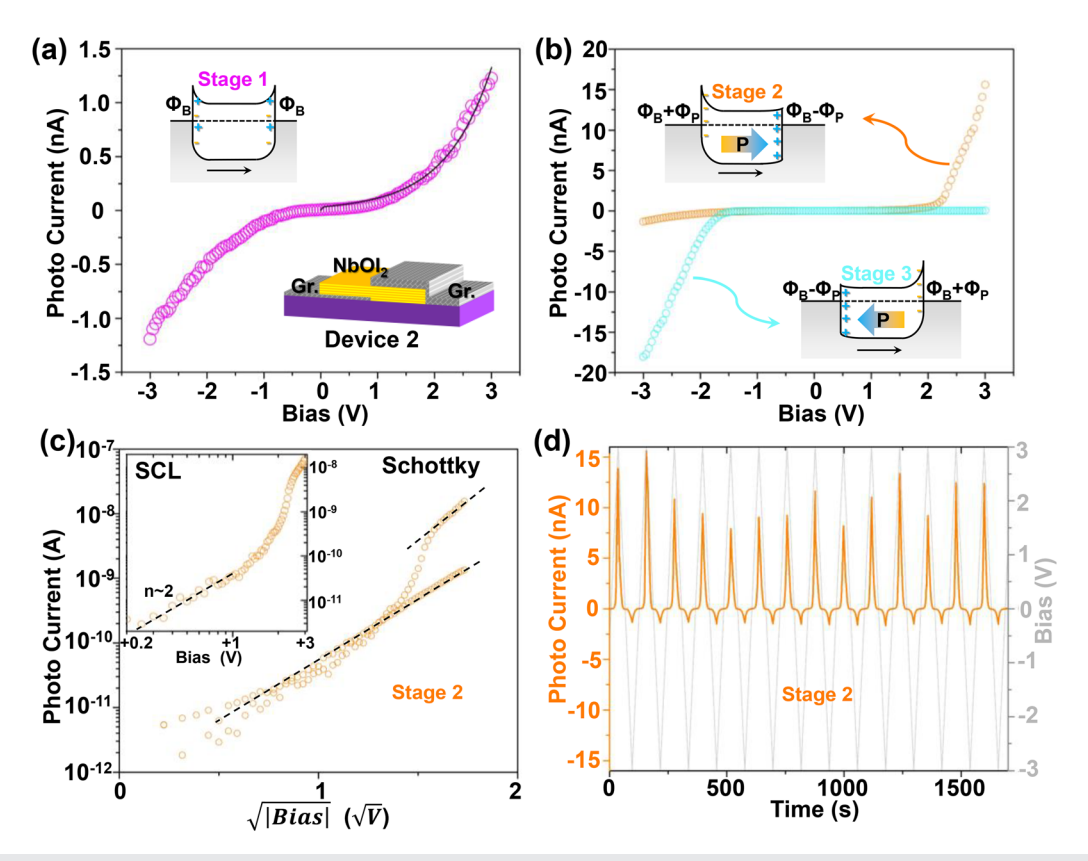


FIG. 4. In-plane ferroelectricity of NbOl₂ probed by the switchable Schottky barriers in device 2. (a) In stage 1, the random dipoles on the interfaces induce symmetric Schottky barriers and, in turn, symmetric photocurrents. (b) With poling, single-Schottky-diode type rectification is observed, whose direction is switchable. (c) Re-plot of I–V curve of stage 2. The main plot using $\log |I| - \sqrt{|V|}$ indicates the Schottky emission in the reverse bias cycle and part of forward bias cycle. The double log re-plot shown in inset indicates SCL conduction in part of forward bias cycle. (d) Repeated I–V scans under stage 2.

indicates that the supposedly asymmetric back-to-back Schottky barriers in stage 2 or 3 are practically dominated by the higher one of the two Schottky barriers. The repeated I–V scans shown in Fig. 4(d) indicate that the rectification observed in stage 2 lasted for over 1500 s, excluding mobile defects as the main cause for the rectification (see Fig. S7 and supplementary material note 5 for details). Similar to the observation in ceramic oxide ferroelectrics, barrier heights can be modulated effectively by illumination, and the switchable rectification of photocurrent along with the symmetric dark current suggests the reported device could be promising in applications that require nonvolatility and reconfigurability.

In summary, we show the feasibility of developing thin NbOI₂ single crystal nanosheets by bulk synthesis and mechanical exfoliation. Based on the transport and optoelectronic studies, Schottky emission is identified as the major conduction mechanism in a \sim 1- μ m-channel NbOI₂ device. By poling the NbOI₂ device with a DC voltage, the photocurrent is changed from symmetric to single-Schottky-diode-like, and the polarity of Schottky rectification is reversed after reversing the DC poling direction. The adjustable Schottky barriers at NbOI₂-graphite interfaces are proposed from the re-alignment of ferroelectric dipoles in NbOI₂. Our work of vdW NbOI₂ sheets may shed light on the design of nonvolatile optoneuromorphic computing and nonvolatile technologies.

See the supplementary material for methods, Figs. S1–S7, and notes 1–5, including AFM, EDX, additional optical images, additional photoresponse transients, ferroelectricity and P–E loop measurements, Schottky barrier measurements, and the analysis on ion migration.

J.S. acknowledges the Air Force Office of Scientific Research under Award No. FA9550-18-1-0116. L.Z. and J.S. acknowledge the NYSTAR Focus Center under Award No. C150117. This work was also partially supported by the National Science Foundation under Award Nos. 1706815, 2024972, 2031692, and 1916652.

The authors declare no competing interest.

DATA AVAILABILITY

The data that support the findings of this study are available from the corresponding author upon reasonable request.

REFERENCES

¹T. P. Ma and J.-P. Han, "Why is nonvolatile ferroelectric memory field-effect transistor still elusive?," IEEE Electron Device Lett. **23**(7), 386–388 (2002).

²A. M. F. Neto and S. R. Salinas, *The Physics of Ferroelectrics: A Modern Perspective* (Springer, 2007).

³M. Si, A. K. Saha, S. Gao, G. Qiu, J. Qin, Y. Duan, J. Jian, C. Niu, H. Wang, W. Wu, S. K. Gupta, and P. D. Ye, "A ferroelectric semiconductor field-effect transistor," Nat. Electron. 2(12), 580–586 (2019).

- ⁴Y. J. Choi, S. Kim, H. J. Woo, Y. J. Song, E. Hwang, M. S. Kang, and J. H. Cho, "Color-selective Schottky barrier modulation for optoelectric logic," ACS Nano 14(11), 16036–16045 (2020).
- ⁵C. Yang, J. Qian, S. Jiang, H. Wang, Q. Wang, Q. Wan, P. K. L. Chan, Y. Shi, and Y. Li, "An optically modulated organic Schottky-barrier planar-diode-based artificial synapse," Adv. Opt. Mater. 8(13), 2000153 (2020).
- ⁶J. Chu, Y. Wang, X. Wang, K. Hu, G. Rao, C. Gong, C. Wu, H. Hong, X. Wang, K. Liu, C. Gao, and J. Xiong, "2D polarized materials: Ferromagnetic, ferrovalley, ferroelectric materials, and related heterostructures," Adv. Mater. 33(5), 2004469 (2021).
- M. Mehboudi, B. M. Fregoso, Y. Yang, W. Zhu, A. van der Zande, J. Ferrer, L. Bellaiche, P. Kumar, and S. Barraza-Lopez, "Structural phase transition and material properties of few-layer monochalcogenides," Phys. Rev. Lett. 117(24), 246802 (2016)
- ⁸R. Fei, W. Kang, and L. Yang, "Ferroelectricity and phase transitions in monolayer group-IV monochalcogenides," Phys. Rev. Lett. **117**(9), 097601 (2016)
- ⁹H. Wang and X. Qian, "Two-dimensional multiferroics in monolayer group IV monochalcogenides," 2D Mater. 4(1), 015042 (2017).
- ¹⁰ M. Wu and X. C. Zeng, "Intrinsic ferroelasticity and/or multiferroicity in two-dimensional phosphorene and phosphorene analogues," Nano Lett. 16(5), 3236–3241 (2016).
- ¹¹Y. Jia, M. Zhao, G. Gou, X. C. Zeng, and J. Li, "Niobium oxide dihalides NbOX₂: New family of two-dimensional van der Waals layered materials with intrinsic ferroelectricity and antiferroelectricity," Nanoscale Horiz. 4(5), 1113–1123 (2019).
- ¹²Y.-Y. Sun, J. Shi, J. Lian, W. Gao, M. L. Agiorgousis, P. Zhang, and S. Zhang, "Discovering lead-free perovskite solar materials with a split-anion approach," Nanoscale 8(12), 6284–6289 (2016).
- ¹³H. Schäfer and F. Kahlenberg, "Beiträge zur Chemie der Elemente Niob und Tantal. XXIV. Bildungsenthalpie, Sättigungsdruck und thermochemisches Verhalten des Nioboxydchlorids NbOCl₃," Z. Anorg. Allg. Chem. 305(5–6), 327–340 (1960).
- ¹⁴J. Rijnsdorp and F. Jellinek, "The crystal structure of niobium oxide diiodide NbOI₂," J. Less-Common Met. 61(1), 79–82 (1978).
- ¹⁵H. Schäber and R. Gerken, "Beiträge zur Chemie der Elemente Niob und Tantal. XXIX. NbOJ₃ und NbOJ₂. Darstellung, Eigenschaften und thermisches Verhalten," Z. Anorg. Allg. Chem. 317, 105–112 (1962).
- ¹⁶H. Ullah, K. Guerin, and P. Bonnet, "Synthesis of Nb₂O₅ nanoplates and their conversion into NbO₂F nanoparticles by controlled fluorination with molecular fluorine," Eur. J. Inorg. Chem. 2019(2), 230–236.
- ¹⁷A. A. McConnell, J. S. Aderson, and C. N. R. Rao, "Raman spectra of niobium oxides," Spectrochim. Acta, Part A 32(5), 1067–1076 (1976).

- ¹⁸R. M. Pittman and A. T. Bell, "Raman studies of the structure of niobium oxide/titanium oxide (Nb₂O₅.TiO₂)," J. Phys. Chem. **97**(47), 12178–12185 (1993).
- ¹⁹H. T. Kreissl, M. M. J. Li, Y.-K. Peng, K. Nakagawa, T. J. N. Hooper, J. V. Hanna, A. Shepherd, T.-S. Wu, Y.-L. Soo, and S. C. E. Tsang, "Structural studies of bulk to nanosize niobium oxides with correlation to their acidity," J. Am. Chem. Soc. 139(36), 12670–12680 (2017).
- ²⁰S. M. Sze and K. K. Ng, *Physics of Semiconductor Devices*, 3rd ed. (Wiley, New York, 2007).
- ²¹D. Lee, S. H. Baek, T. H. Kim, J. G. Yoon, C. M. Folkman, C. B. Eom, and T. W. Noh, "Polarity control of carrier injection at ferroelectric/metal interfaces for electrically switchable diode and photovoltaic effects," Phys. Rev. B 84(12), 125305 (2011).
- ²²Y. Zheng, J. Gao, C. Han, and W. Chen, "Ohmic contact engineering for two-dimensional materials," Cell Rep. Phys. Sci. 2(1), 100298 (2021).
- 23Y. Fan, Y. Zhou, X. Wang, H. Tan, Y. Rong, and J. H. Warner, "Photoinduced Schottky barrier lowering in 2D monolayer WS₂ photodetectors," Adv. Opt. Mater. 4(10), 1573–1581 (2016).
- ²⁴T. Choi, S. Lee, Y. J. Choi, V. Kiryukhin, and S.-W. Cheong, "Switchable ferroelectric diode and photovoltaic effect in BiFeO₃," Science 324(5923), 63–66 (2009).
- 25N. Higashitarumizu, H. Kawamoto, C.-J. Lee, B.-H. Lin, F.-H. Chu, I. Yonemori, T. Nishimura, K. Wakabayashi, W.-H. Chang, and K. Nagashio, "Purely in-plane ferroelectricity in monolayer SnS at room temperature," Nat. Commun. 11(1), 2428 (2020).
- 26T. Nagano, M. Tsutsui, R. Nouchi, N. Kawasaki, Y. Ohta, Y. Kubozono, N. Takahashi, and A. Fujiwara, "Output properties of C₆₀ field-effect transistors with Au electrodes modified by 1-alkanethiols," J. Phys. Chem. C 111(19), 7211–7217 (2007).
- ²⁷C. Wang, M. Takahashi, H. Fujino, X. Zhao, E. Kume, T. Horiuchi, and S. Sakai, "Leakage current of multiferroic (Bi_{0.6}Tb_{0.3}La_{0.1})FeO₃ thin films grown at various oxygen pressures by pulsed laser deposition and annealing effect," J. Appl. Phys. 99(5), 054104 (2006).
- ²⁸D. Song, J. Yang, B. Yang, L. Chen, F. Wang, and X. Zhu, "Evolution of structure and ferroelectricity in Aurivillius Bi₄Bi_{n-3}Fe_{n-3}Ti₃O_{3n+3} thin films," J. Mater. Chem. C 6(32), 8618–8627 (2018).
- ²⁹Z. Xiao, Y. Yuan, Y. Shao, Q. Wang, Q. Dong, C. Bi, P. Sharma, A. Gruverman, and J. Huang, "Giant switchable photovoltaic effect in organometal trihalide perovskite devices," Nat. Mater. 14(2), 193–198 (2015).
- ³⁰Q. Dong, J. Song, Y. Fang, Y. Shao, S. Ducharme, and J. Huang, "Lateral-structure single-crystal hybrid perovskite solar cells via piezoelectric poling," Adv. Mater. 28(14), 2816–2821 (2016).
- ³¹G. Vats, J. Peräntie, J. Palosaari, J. Juuti, J. Seidel, and Y. Bai, "Current modulation by optoelectric control of ferroelectric domains," ACS Appl. Electron. Mater. 2(9), 2829–2836 (2020).